Nano Research

Open Access

Research Article

Substitution energy-guided screening of diffusion barrier materials for Ag_2Se-based thermoelectric coolers

Shiyuan Zhao[1,§], Xiao-Lei Shi[2,§], Qi Zhou[1], Zhongwei Zhang[1], Jisheng Liang[1], Zhengniu Pan[1], Sijing Zhu[1], Meng Li[2], Wenyi Chen[2], Jun-Liang Chen[3], Jie Gao[3], Tomohiro Sato[4], Lei Miao[1] ✉, and Zhi-Gang Chen[2] ✉

[1] *Guangxi Novel Battery Materials Research Centre of Engineering Technology, School of Physical Science and Technology, Guangxi University, Nanning 530004, China*
[2] *School of Chemistry and Physics, ARC Research Hub in Zero-emission Power Generation for Carbon Neutrality, Centre for Materials Science, Queensland University of Technology, Brisbane, Queensland 4000, Australia*
[3] *Guangxi Key Laboratory of Information Materials, Engineering Research Centre of Electronic Information Materials and Devices, Ministry of Education, Guilin University of Electronic Technology, Guilin 541004, China*
[4] *Sinter Land Inc., 123 Amaike, Nagaoka, Niigata 940-2055, Japan*
§ *Shiyuan Zhao and Xiao-Lei Shi contributed equally to this work.*

Cite this article: *Nano Research*, **2025**, *18*, 94907903. https://doi.org/10.26599/NR.2025.94907903

ABSTRACT: Diffusion barrier materials (DBMs) are critical for the stability and efficiency of thermoelectric devices. Conventional DBM selection via density functional theory (DFT) calculations is computationally intensive. Here, we introduce an efficient screening approach that employs substitution energy as a surrogate for interfacial reaction energy, significantly reducing computational demand. By integrating substitution energy with migration energy barriers, we identify Ni as a robust DBM for Ag_2Se. Experimental validation confirms that Ni/Ag_2Se joints exhibit low contact resistivity (6.6 μΩ·cm²) and high thermal stability after 30 days of thermal aging. The Te-free Ag_2Se/MgAgSb devices achieve a maximum cooling temperature difference of 68 K at 350 K, comparable to state-of-the-art Ag_2Se/Bi_2Te_3 devices, while demonstrating excellent durability over 2000 power cycles. This strategy offers a rapid and reliable framework for DBM selection, accelerating the advancement of high-performance thermoelectric devices.

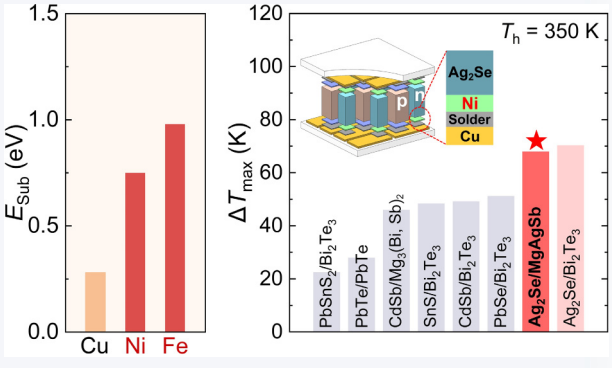

KEYWORDS: thermoelectric, Ag_2Se, device, diffusion barrier, substitution energy

1 Introduction

Thermoelectric (TE) technology enables the direct conversion between heat and electricity based on the Seebeck and Peltier effects, and can be used for both power generation and refrigeration [1–5]. Thermoelectric materials and devices offer several advantages, including compact size, low noise, maintenance-free operation, and precise temperature control, making them highly promising for applications, such as space power systems, industrial waste heat recovery, portable cooling devices, and thermal management in electronic equipment [6–8]. In particular, the growing demand for precise thermal regulation in areas, such as power batteries, laser diodes, infrared detectors, and temperature-controlled clothing has significantly advanced thermoelectric cooling technologies [9–11]. In general, thermoelectric materials form the core of thermoelectric devices. The higher the thermoelectric performance of the material (typically evaluated by the dimensionless figure of merit (ZT)), the greater the theoretical efficiency of the device in power generation or cooling [12, 13]. Over the past few decades, significant progress in the understanding of thermoelectric physics and chemistry, along with advanced strategies involving composition optimization based on band engineering and micro/nanostructure engineering, has led to a substantial increase in ZT, thus driving the development of high-performance thermoelectric devices [14–16]. However, compared to the rapid improvement in material performance, the development of thermoelectric devices has lagged. One major

Received: August 2, 2025; **Revised:** August 6, 2025
Accepted: August 6, 2025

✉Address correspondence to Lei Miao, miaolei@gxu.edu.cn; Zhi-Gang Chen, zhigang.chen@qut.edu.au

challenge lies in designing reliable diffusion barrier materials (DBMs) [17, 18]. DBMs play a critical role in preventing interdiffusion and chemical reactions between the thermoelectric material and the electrode, while also ensuring low interfacial contact resistivity (ρ_c) and strong mechanical bonding during long-term operation. As such, the performance stability and structural reliability of thermoelectric devices largely depend on the effectiveness of the DBM [19–21].

Traditionally, the selection of DBMs has been based on empirical approaches. This typically involves selecting pure metals or multicomponent alloys as potential DBM candidates, guided by criteria, such as matching thermal expansion coefficients for strong interfacial bonding and aligned work functions for low ρ_c. Subsequently, long-term thermal aging tests of fabricated thermoelectric joints (DBM/thermoelectric material) are conducted to evaluate interfacial stability [22–24]. However, this trial-and-error method is both time-consuming and labor-intensive, and often fails to achieve highly stable bonded interfaces. In recent years, several more precise strategies for DBM screening have been proposed, including high-throughput methods [25–27], phase diagram calculations [19, 28–31], and density functional theory (DFT) simulations [31–34]. Among them, the DFT-based strategy is grounded in the theory of solid-state diffusion reactions [32]. It involves calculating the interface reaction energy (E_{IR}) between DBM candidates and thermoelectric materials, as well as the migration energy barrier (E_{Mig}) of diffusing atoms. Generally, a lower E_{IR} indicates more severe interfacial reactions, while a larger E_{Mig} suggests slower growth of the reaction layer during prolonged device operation. Therefore, suitable DBMs are typically screened based on having an E_{IR} close to zero and a sufficiently large E_{Mig} [31–33]. However, a key limitation of this approach is the potential formation of multiple interfacial reaction products. Since the actual reaction products cannot be precisely predicted, it is necessary to calculate the E_{IR} for all possible reactions, resulting in a substantial computational burden.

In substitution-type interfacial reactions (A + BC → AC + B), particularly those occurring between pure metals and metal chalcogenides (e.g., Ag_2Q and Cu_2Q, where Q = S, Se, and Te), the high electronegativity of chalcogens (S: 2.58, Se: 2.55, and Te: 2.10) drives their preferential bonding with most pure metals. This often results in the formation of stable compounds and the precipitation of Ag or Cu. Accordingly, the chemical reactivity of DBM candidates can be assessed based on the substitution energy (E_{Sub}) of DBM atoms replacing Ag or Cu atoms in the host lattice. A lower E_{Sub} indicates a more energetically favorable substitution reaction, suggesting a higher likelihood of interfacial reactivity, consistent with trends predicted by E_{IR}. The E_{Sub}-based screening approach enables efficient evaluation of chemical compatibility between DBMs and metal chalcogenides, requiring only a single substitution energy calculation without the need to explore all possible reaction pathways.

In this study, n-type Ag_2Se thermoelectric material is investigated as a representative case [35, 36]. Ag_2Se has emerged in recent years as a promising, low-cost alternative to the commercially dominant Bi_2Te_3, owing to its comparable near-room-temperature thermoelectric performance (ZT = 1) and the significantly lower cost of Se compared to Te [37–46]. Despite its potential, the device-level development of Ag_2Se has progressed relatively slowly. One major reason is the lack of research on suitable DBMs for use in Ag_2Se-based devices. Given that interfacial reactions between pure metals and Ag_2Se are typically substitution reactions, we adopt the more computationally efficient E_{Sub} instead of the more complex E_{IR}. Based on the E_{Sub} of DBM atoms substituting Ag sites in the Ag_2Se lattice, and the E_{Mig} for DBM atoms diffusing into neighbouring Ag vacancies, we rapidly identify Ni as a promising DBM candidate. Experimental results confirm that Ni/Ag_2Se joints maintain a stable interfacial structure during long-term thermal aging and exhibit low ρ_c. A device comprising seven pairs of Ag_2Se/MgAgSb legs, with Ni employed as the DBM for the Ag_2Se legs, demonstrates excellent cooling performance and high reliability. Our work not only highlights the significant practical potential of Ag_2Se-based thermoelectric devices but also provides a feasible and efficient strategy for the screening of effective DBMs.

2 Results and discussion

2.1 The screening strategy of DBMs

The melting point (T_m) and wettability were employed as preliminary criteria to screen 14 conventional DBM metals. In this study, we used nanoscale metal powders (less than 500 nm) combined with a one-step sintering method to rapidly fabricate dense DBM/Ag_2Se/DBM joints. Previous research on spark plasma sintering (SPS) has shown that nanoscale metal powders can be densified into bulk materials at temperatures above approximately 0.3 T_m, owing to their high specific surface area and surface energy [47, 48]. Given the sintering temperature (T_s) range of Ag_2Se (135 to 500 °C) [41, 49, 50], suitable DBM metals should have a T_m below 1667 °C (Fig. 1(a)). In addition, good wettability between the DBM and the solder is essential for forming strong connections between the thermoelectric legs and the electrodes. The contact angle (θ) between the metal and the solder is a key parameter for evaluating wettability; generally, a contact angle less than 40° indicates good wettability and solderability [51]. Reported θ values for various solders on different metal substrates are summarized in Fig. 1(a) [52–61]. Based on the considerations of T_m and wettability, Cu, Ag, Ni, and Fe were selected as promising DBM candidates.

According to diffusion reaction theory, the growth of the interfacial reaction layer (IRL) is governed by two sequential processes: chemical reaction and atomic diffusion [32]. As illustrated in Fig. 1(b), when the DBM comes into contact with Ag_2Se at elevated temperatures, a chemical reaction first occurs, forming a thin IRL. The time required for this initial chemical reaction typically exceeds that of atomic diffusion, indicating that the early-stage IRL growth is reaction-controlled. The interfacial reactions between pure metals and Ag_2Se mainly involve atomic substitution. Given that Ag sites in Ag_2Se exhibit the lowest vacancy formation energy (Table S1 in the Electronic Supplementary Material (ESM)), DBM atoms are energetically favored to diffuse into the Ag sublattice of Ag_2Se. Therefore, the E_{Sub} of DBM atoms at Ag sites in the Ag_2Se lattice can be used to evaluate the interfacial reactivity. In general, a lower E_{Sub} indicates that the interfacial reactions are more likely to occur. As the reaction progresses and the immediate reactant atoms near the interface become depleted, the continued growth of the IRL is dominated by the diffusion of DBM atoms into the Ag_2Se lattice. Accordingly, the E_{Mig} for DBM atoms moving from an Ag site to a neighboring Ag vacancy can be used to assess the diffusion rate. A lower E_{Mig} corresponds to faster atomic diffusion, leading to more rapid IRL growth. Therefore, DBM candidates were further screened based on the following

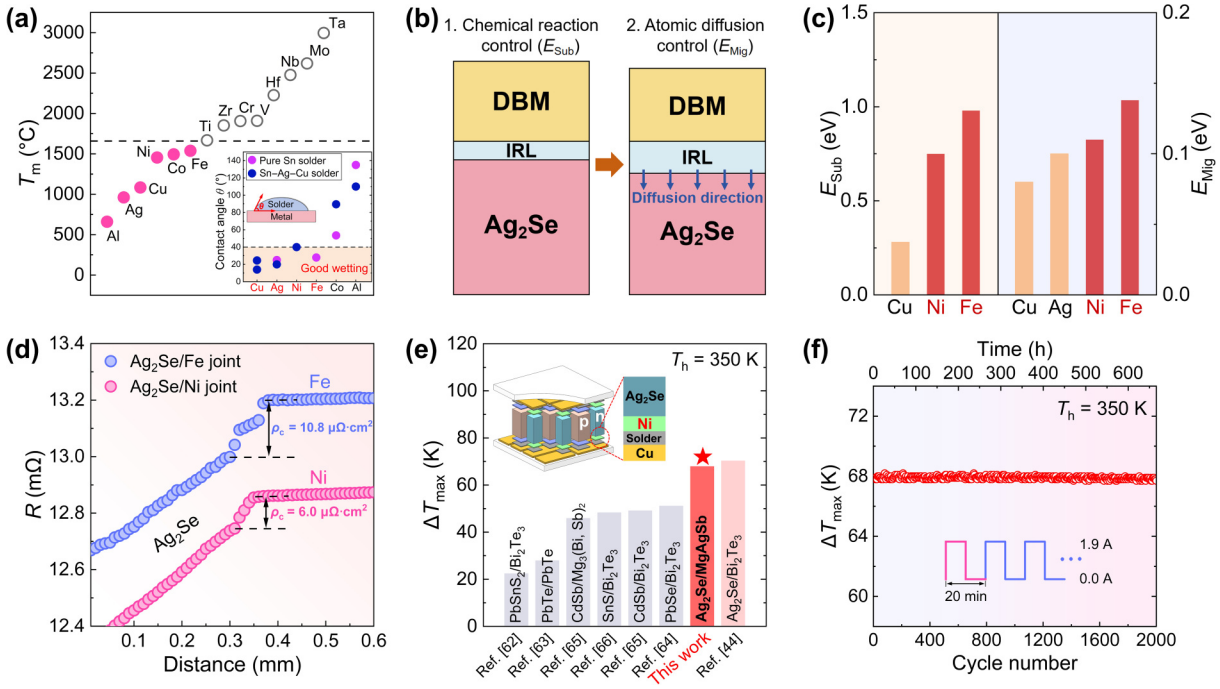

Figure 1 Screening strategy of DBM and the excellent Ag_2Se/MgAgSb cooler. (a) T_m of 14 conventional DBM metals. Insets: the reported θ of various solders on different metal substrates [52–61] and the schematic diagram for measuring θ. (b) Schematic model of IRL growth. The E_{Sub} and E_{Mig} are the crucial parameters in controlling IRL growth. (c) E_{Sub} and E_{Mig} of DBM candidates (Cu, Ag, Ni, and Fe) by DFT calculations. (d) ρ_c of the as-sintered Ag_2Se/Fe joint and Ag_2Se/Ni joint. (e) Comparison of the ΔT_{max} of our Ag_2Se/MgAgSb thermoelectric cooler with those of previously reported coolers at T_h of 350 K [44, 62–66]. Inset: the schematic diagram of Ag_2Se/MgAgSb cooler. (f) ΔT_{max} of the Ag_2Se/MgAgSb cooler throughout power cycling tests at T_h = 350 K. Inset: the cycling current regime, where the input current cycles between 1.9 and 0.0 A.

criteria: a sufficiently large E_{Sub} to suppress interfacial reactivity and a high E_{Mig} to slow down IRL growth.

Based on the calculated E_{Sub} (Fig. 1(c) and Fig. S1(a) in the ESM), Cu, with its low E_{Sub}, is predicted to react readily with Ag_2Se, while Ni and Fe exhibit progressively weaker chemical reactivity. It is worth noting that Ag does not react with Ag_2Se, and therefore its E_{Sub} is not defined. Next, we evaluated the E_{Mig} for three distinct atomic diffusion pathways from Ag sites to neighboring Ag vacancies in Ag_2Se (Figs. S1(b) and S1(c) in the ESM). Among these, channel 3 was found to have the lowest migration energy barrier and was thus selected as the representative diffusion pathway for DBM atoms in the Ag_2Se lattice. As shown in Fig. 1(c) and Fig. S1(d) in the ESM, both Cu and Ag exhibit low E_{Mig} values, indicating higher diffusion rates within the Ag_2Se lattice. In contrast, Ni and Fe show significantly higher E_{Mig}, suggesting slower diffusion and, consequently, a slower growth rate of the interfacial reaction layer. Combining the results of E_{Sub} and E_{Mig}, Ni and Fe emerge as promising DBM candidates. To experimentally validate this, we measured the ρ_c of Ag_2Se/Ni and Ag_2Se/Fe joints (Fig. 1(d)). The Ag_2Se/Ni interface exhibited a lower ρ_c of 6.0 μΩ·cm², leading to the selection of Ni as the DBM for the Ag_2Se-based device. Using Ni as the DBM, a Te-free Ag_2Se/MgAgSb thermoelectric cooler was fabricated, achieving a maximum temperature difference (ΔT_{max}) of 68 K at a hot-side temperature (T_h) of 350 K. This performance surpasses that of $PbSnS_2$ [62], PbX (X = Te/Se) [63, 64], CdSb [65], and SnS-based [66] thermoelectric coolers, and is comparable to that of advanced Ag_2Se/Bi_2Te_3-based coolers [44] (Fig. 1(e)). Furthermore, the ΔT_{max} of the Ag_2Se/MgAgSb cooler remained virtually unchanged after 2000 power cycling tests, demonstrating excellent long-term stability (Fig. 1(f)).

2.2 Experimental verification of the screening strategy

To verify the reliability of the screening results, DBM/Ag_2Se/DBM joints were fabricated using the one-step sintering method illustrated in Fig. 2(a). The glass fiber filter and polyimide film used in the graphite mold acted as electrical insulators, preventing the uneven distribution of Ag^+ ions under high current and elevated temperatures. The sintering conditions for the Cu/Ag_2Se/Cu, Ni/Ag_2Se/Ni, and Ag/Ag_2Se/Ag joints were set at 623 K for 5 min. Given the higher T_m of Fe, the T_s and holding time for the Fe/Ag_2Se/Fe joints were increased to 673 K and 10 min, respectively. As shown in Fig. 2(b), a strong chemical reaction and extensive elemental diffusion occurred between Cu and Ag_2Se, resulting in the near-complete consumption of the outer Cu layer. Simultaneously, a significant amount of CuAgSe secondary phases and Ag precipitates formed within the Ag_2Se matrix, as confirmed by energy dispersive spectrometer (EDS) elemental analysis and X-ray diffraction (XRD) patterns (Figs. S2 and S3 in the ESM). These results indicate that Cu is highly reactive with Ag_2Se. For the Ni/Ag_2Se joint, a well-defined interface is observed (Fig. 2(c)), with two IRLs (Ni_3Se_2 and NiSe) forming at the junction, with a combined thickness of approximately 50 μm (Figs. S4 and S5 in the ESM). Similarly, an FeSe reaction layer of about 40 μm is formed at the Fe/Ag_2Se interface (Fig. 2(d) and Fig. S6 in the ESM), which is thinner than that at the Ni/Ag_2Se interface. However, due to the relatively lower T_s for Fe, the Fe/Ag_2Se interface exhibits residual Fe particles, numerous voids, and microcracks, leading to a high ρ_c of 10.8 μΩ·cm² (Fig. 1(d)). While increasing T_s could potentially eliminate these interfacial defects, it was found that the thermoelectric performance of Ag_2Se deteriorated after sintering at 723 K (Fig. S7 in the ESM). Therefore, higher T_s values were not

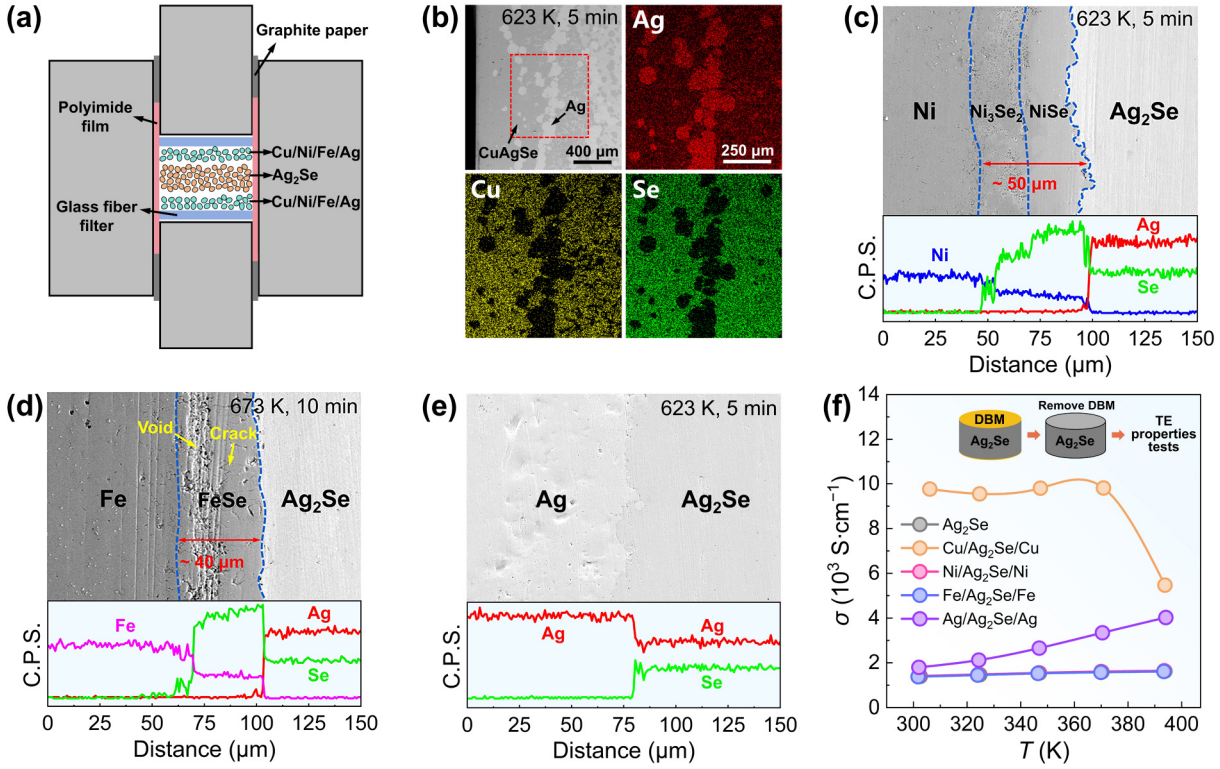

Figure 2 Experimental verification for four DBM candidates. (a) Schematic diagram of DBM/Ag_2Se/DBM joints by one-step sintering method. ((b)–(e)) SEM images, EDS elemental mapping and line scanning results of (b) Cu, (c) Ni, (d) Fe, and (e) Ag with Ag_2Se at different sintering temperatures and holding times. C.P.S. stands for: counts per second. (f) σ of Ag_2Se after DBM removal. Inset: schematic diagram of removing the external DBM layers from the as-sintered joints.

pursued for Fe/Ag_2Se joints. In contrast, the Ag/Ag_2Se interface is exceptionally clean, free of reaction products, and represents an ideal interface condition (Fig. 2(e)). However, EDS analysis revealed partial diffusion of Ag from the electrode into the Ag_2Se, thereby altering the initial Ag:Se atomic ratio (Fig. S8 in the ESM). Overall, the experimentally observed interfacial reactions and diffusion behaviors in the four types of thermoelectric joints are consistent with the calculated E_{Sub} and E_{Mig} values, thereby validating the accuracy and effectiveness of our DBM screening strategy.

In addition, to assess the impact of the four DBM metals on the thermoelectric properties of Ag_2Se, we removed the external DBM layers from the sintered joints and measured the thermoelectric properties of the exposed Ag_2Se material. As shown in Fig. 2(f) and Fig. S9 in the ESM, extensive diffusion of Cu and Ag into the Ag_2Se matrix led to an increase in carrier concentration. Consequently, the room-temperature electrical conductivity (σ) of the Cu/Ag_2Se/Cu sample reached 9762 S·cm^{-1}, while that of the Ag/Ag_2Se/Ag sample increased from 1800 to 4026 S·cm^{-1} with rising temperature. As a result, the ZT values of both samples decreased significantly, consistent with previous reports on Cu doping and Ag-rich compositions in Ag_2Se [67–70]. In contrast, Ni and Fe showed limited interfacial reactions and minimal elemental diffusion into Ag_2Se, thereby preserving the intrinsic thermoelectric properties of the material.

2.3 Interfacial properties and stability of the Ni/Ag_2Se joint

To verify the effectiveness of Ni as a DBM for Ag_2Se, the interfacial properties of Ni/Ag_2Se joints were thoroughly investigated. Considering that the operating temperature of thermoelectric coolers typically does not exceed 353 K, we conducted accelerated thermal aging experiments to evaluate the long-term interfacial stability within a shortened experimental timeframe. Specifically, Ni/Ag_2Se joints were aged at 398 K for 30 days, during which changes in the interfacial microstructure and properties were systematically monitored. After 30 days of thermal aging, the IRL at the Ni/Ag_2Se interface showed merely a ~ 5 μm thickness increment relative to the initial state (Fig. 3(a) and Fig. S10 in the ESM), while remaining composed of Ni_3Se_2 and NiSe phases (Fig. 3(b) and Fig. S11 in the ESM). Moreover, the IRL growth rate progressively decreased over time. As shown in Fig. 3(c) and Fig. S12 in the ESM, the average ρ_c of the as-sintered Ni/Ag_2Se joint was 6.0 μΩ·cm^2, which increased slightly to 6.6 μΩ·cm^2 after 30 days of thermal aging (Table S3 in the ESM). This minor increase in ρ_c correlates with the moderate thickening of the IRL. The linear current–voltage (I–V) characteristics observed in both as-sintered and aged Ni/Ag_2Se joints confirm the formation of Ohmic contacts at all interfaces (Fig. 3(d)), contributing to the low ρ_c of the Ni/Ag_2Se joint. Notably, both the IRL thickness and ρ_c exhibited a linear relationship with the square root of the aging time (Fig. S13 in the ESM), indicating that the interfacial evolution at 398 K is governed by a diffusion-controlled mechanism [71, 72]. Furthermore, the shear strength (σ_s) of the Ni/Ag_2Se interface increased gradually over the aging period and remained above 10 MPa (Fig. 3(c) and Fig. S14 in the ESM), meeting the mechanical strength requirements for reliable device operation [22]. As shown in Fig. 3(e) and Fig. S15 in the ESM, the coefficients of thermal expansion (CTEs) of NiSe and Ni_3Se_2 lie between those of Ag_2Se and Ni. This suggests that the Ni_3Se_2/NiSe interlayers effectively buffer thermal stresses during operation, thereby mitigating stress concentration and preventing interfacial failure. Finite element

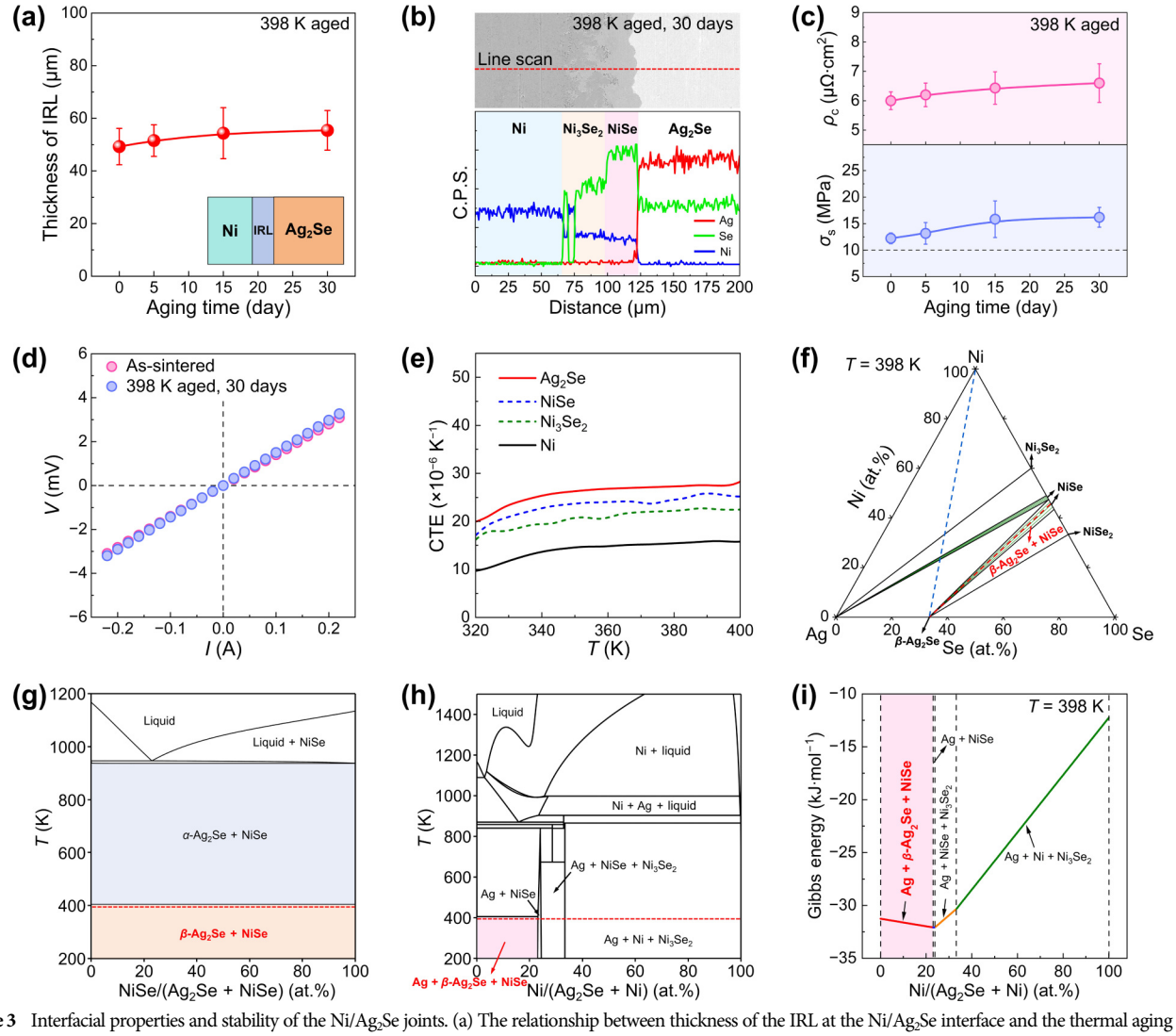

Figure 3 Interfacial properties and stability of the Ni/Ag_2Se joints. (a) The relationship between thickness of the IRL at the Ni/Ag_2Se interface and the thermal aging time. (b) SEM image and EDS line scanning results of the Ni/Ag_2Se joint after thermal aging at 398 K for 30 days. (c) Measured ρ_c and σ_s as a function of the aging time at 398 K. The marks and error bars for ρ_c and σ_s represent the average values and standard deviations of three parallel samples. (d) *I*–*V* curves of as-sintered and aged Ni/Ag_2Se joint at 398 K for 30 days. (e) The CTE of Ag_2Se, NiSe, Ni_3Se_2 and Ni. (f) Calculated isothermal section at 398 K of the Ag–Ni–Se ternary phase diagram. (g) Calculated vertical section of Ag_2Se–NiSe phase diagram. (h) Calculated vertical section of Ag_2Se–Ni phase diagram. (i) Calculated Gibbs energies for Ag_2Se–Ni at 398 K.

simulations of von Mises stress quantitatively confirm this effect, showing that the Ni_3Se_2/NiSe interlayer reduces interfacial thermal stress by approximately 19% compared to a direct Ni/Ag_2Se interface (Fig. S16 in the ESM), thereby validating the stress-buffering role of the interfacial Ni_3Se_2 and NiSe phases.

The long-term stability of the Ni/Ag_2Se interface can be attributed to two key factors: (i) the high E_{Sub} and E_{Mig} of Ni atoms in the Ag_2Se lattice, and (ii) the thermodynamic phase equilibrium between the NiSe compound and Ag_2Se. To investigate this further, we consulted the available thermodynamic data from the Ag–Ni [73], Ag–Se [74], and Ni–Se [75] binary phase diagrams and subsequently calculated the isothermal section of the Ag–Ni–Se ternary phase diagram at 398 K using Pandat software (Fig. 3(f) and Fig. S17 in the ESM). The phase diagram reveals a two-phase equilibrium region consisting of β-Ag_2Se and NiSe. A vertical section was taken along the compositional tie-line connecting β-Ag_2Se and NiSe (red dashed line in Fig. 3(f)), yielding the equilibrium phase diagram of the Ag_2Se–NiSe system across various temperatures and atomic ratios (Fig. 3(g)). Within the temperature range from room temperature to 398 K, no chemical reaction occurs between β-Ag_2Se and NiSe, regardless of NiSe composition, confirming their thermodynamic compatibility. We further examined a vertical section along the tie-line between β-Ag_2Se and Ni (blue dashed line in Fig. 3(f)), from which the equilibrium phase diagram of the Ag_2Se–Ni system was derived (Fig. 3(h)). At 398 K, four possible interfacial reaction structures may form as the Ni content increases: Ag + Ag_2Se + NiSe, Ag + NiSe, Ag + NiSe + Ni_3Se_2, and Ag + Ni + Ni_3Se_2. The Gibbs free energies of these four configurations were calculated at 398 K (Fig. 3(i)). Among them, the Ag + Ag_2Se + NiSe system exhibits the lowest Gibbs energy, indicating thermodynamic stability and a low propensity for further interfacial reactions. These results suggest that the *in situ* formation of NiSe at the Ni/Ag_2Se interface plays a crucial role in suppressing interfacial reactions and ensuring the long-term thermal stability of the joint.

This E_{Sub}-based screening strategy was also successfully applied to p-type Cu_2Se thermoelectric materials. The interfacial reactions observed for four DBM candidates (Ag, Co, Ni, and Fe) with Cu_2Se

were consistent with the calculated E_{Sub} values (Figs. S18–S20 in the ESM). Taking into account both interfacial thermal stability and post-aging ρ_c, Ni was identified as the optimal DBM for Cu_2Se-based devices (Figs. S21 and S22 in the ESM).

2.4 Thermoelectric cooler design and performance evaluation

Efficient and reliable thermoelectric devices require both p- and n-type materials with high ZT values, along with stable, low-resistance (R) interfacial connections. In this study, we selected p-type MgAgSb to pair with n-type $Ag_2Se_{1.08}$ (hereafter referred to as Ag_2Se) to fabricate a Te-free thermoelectric cooler. By employing different synthesis methods (Fig. S23 in the ESM), we successfully prepared Ag_2Se and MgAgSb materials, both exhibiting ZT values above 0.8 at room temperature (Fig. 4(a) and Fig. S24 in the ESM). Moreover, in the temperature range of 300–350 K, the ZT values of the two materials are well-matched, indicating excellent compatibility in performance. To ensure reliable electrical and mechanical connections between the p-type legs and electrodes, traditional Ag was employed as the DBM for MgAgSb. A detailed investigation of the Ag/MgAgSb interface revealed that it maintained a strong bond after 30 days of thermal aging at 398 K, with no IRL observed, confirming excellent thermal stability (Fig. S25 in the ESM). Furthermore, the ρ_c of the Ag/MgAgSb interface remained low at 11.4 μΩ·cm² after aging (Fig. S26 in the ESM).

Based on the thermoelectric properties of the materials and the measured ρ_c, finite element simulations were conducted to optimize the geometric dimensions of the thermoelectric legs. The simulation results indicate that achieving the ΔT_{max} requires an optimal cross-sectional area ratio of p-type to n-type legs (A_p/A_n) of approximately 1.7, and a leg height (H) greater than 3.2 mm (Fig. 4(b)). Accordingly, we designed the leg dimensions with A_p = 1.7 mm × 1.7 mm, A_n = 1.3 mm × 1.3 mm, and fixed H at 3.3 mm in the fabricated thermoelectric cooler. Figure 4(c) demonstrates the multiple-layer structure and dimension of the Ag_2Se/MgAgSb cooler. The temperature difference (ΔT), cooling power (Q_c), and coefficient of performance (COP) of the device were measured using a commercial testing apparatus (Fig. S28 in the ESM). At optimal current conditions, the cooler achieved ΔT_{max} values of 52, 58, and 68 K at T_h of 300, 323, and 350 K, respectively (Fig. 4(d)).

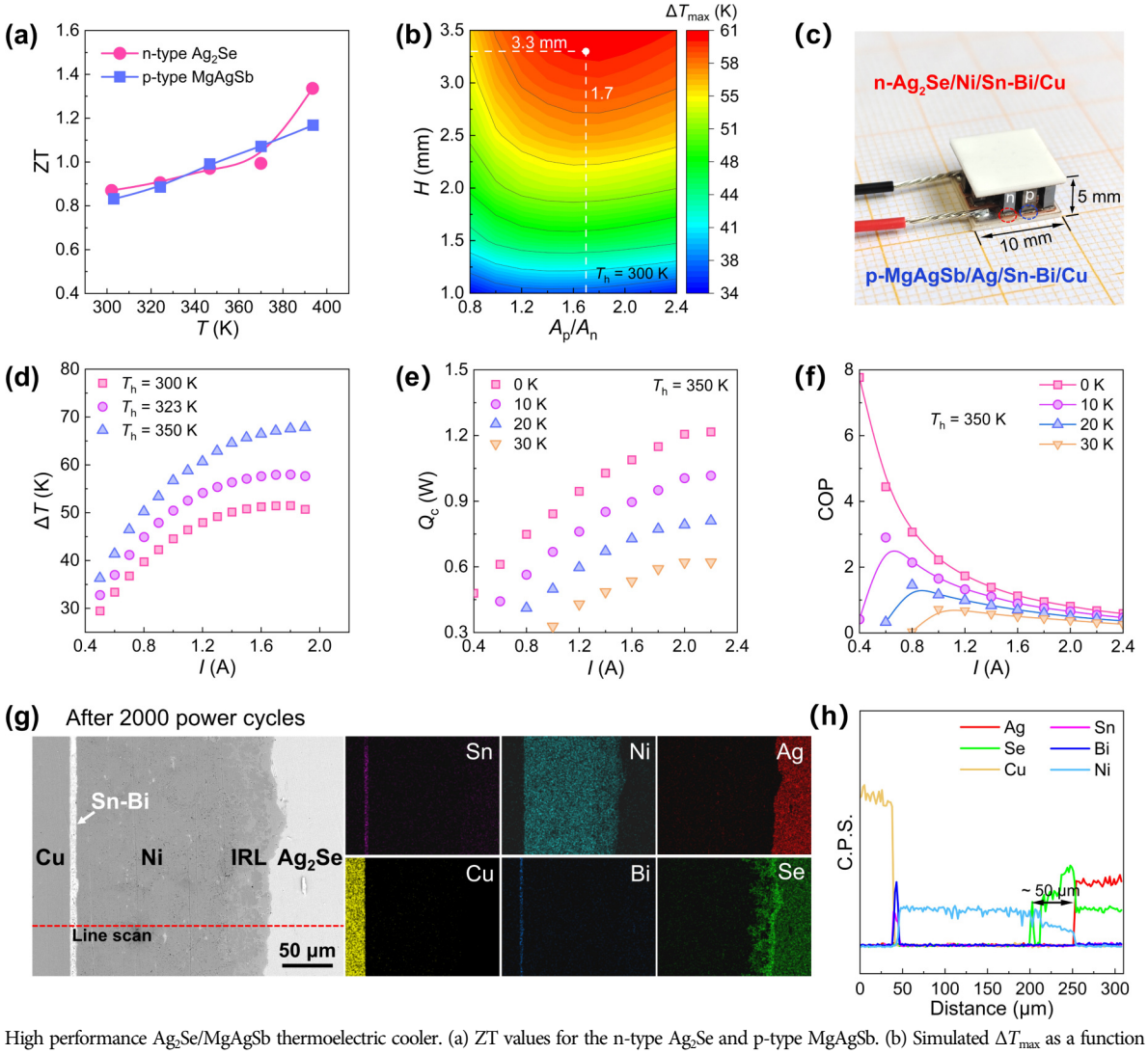

Figure 4 High performance Ag_2Se/MgAgSb thermoelectric cooler. (a) ZT values for the n-type Ag_2Se and p-type MgAgSb. (b) Simulated ΔT_{max} as a function of the H and the A_p/A_n. (c) Photograph of the fabricated Ag_2Se/MgAgSb thermoelectric cooler. (d) I–dependent ΔT at the T_h = 300, 323, and 350 K. (e) Q_c and (f) COP as a function of I at different temperature differences at T_h = 350 K. (g) Cross-sectional SEM image, EDS mapping, and (h) EDS line scans of the hot-side interface of the soldered Ag_2Se leg with Cu electrode after 2000 power cycles.

When the ΔT between the hot and cold sides is 0 K, the Ag_2Se/MgAgSb cooler delivers a maximum cooling power ($Q_{c,max}$) of 1.2 W at T_h = 350 K (Fig. 4(e)), corresponding to a cooling power density of 1.2 W·cm^{-2}. The COP, defined as the ratio of Q_c to the input electrical power, was also evaluated. At T_h = 350 K, the maximum COP values at ΔT of 0, 10, and 20 K were 7.8, 2.9, and 1.5, respectively (Fig. 4(f)). Additional Q_c and COP data at T_h = 300 and 323 K are provided in Fig. S29 in the ESM.

In addition, power cycling tests were performed to assess the long-term stability of the Ag_2Se/MgAgSb thermoelectric cooler. During the tests, the input current was alternated between 0 and 1.9 A in 20 min cycles, while the T_h was maintained at 350 K. As shown in Fig. 1(f) and Fig. S30 in the ESM, both the ΔT_{max} and the internal resistance (R_{in}) of the cooler remained remarkably stable over 2000 power cycles. This outstanding long-term stability is largely attributed to the robust Ni/Ag_2Se interface. As shown in Fig. 4(g), cross-sectional scanning electron microscopy (SEM) image of the soldered Ag_2Se leg with a Cu electrode confirms that all interfaces remain well bonded, with no cracks or voids observed after power cycles. EDS elemental mapping and line scanning results (Fig. 4(h)) demonstrate that the IRL at the Ag_2Se/Ni interface remains approximately 50 μm thick, consistent with the as-sintered state (Fig. 2(c)), indicating minimal interfacial degradation. Moreover, the IRL after cycling still contains NiSe and Ni_3Se_2 phases (Fig. S31 in the ESM). Further confirmation of device stability was obtained through current shock tests on the Ag_2Se material. As shown in Figs. S32(a) and S32(b) in the ESM, both the σ and Seebeck coefficient (S) of Ag_2Se remained virtually unchanged when subjected to increasing current densities from 0 to 80 A·cm^{-2}. Due to Joule heating, the material temperature rose to approximately 360 K (Fig. S32(c) in the ESM). EDS analysis confirmed uniform distribution of Ag and Se elements even after exposure to the highest current density (Fig. S32(d) in the ESM), demonstrating that the Ag_2Se material maintains its structural and electrical integrity under combined thermal and electrical stress, as long as the operating temperature remains below its phase transition point (407 K).

3 Conclusions

In summary, this study presents a streamlined approach for DBM screening in metal chalcogenide-based devices, adopting E_{Sub} as a simplified criterion within the conventional DFT-based framework. Using Ag_2Se as a case study, Ni was identified as a reliable DBM for Ag_2Se-based devices. The Ni/Ag_2Se interface maintains a stable reaction layer thickness and low ρ_c after 30 days of accelerated thermal aging. This excellent stability is attributed to Ni's low chemical reactivity, limited atomic diffusion in Ag_2Se, and the thermodynamic equilibrium between NiSe and Ag_2Se. As a result, the Ag_2Se/MgAgSb thermoelectric cooler demonstrates a high ΔT_{max} and outstanding long-term reliability during power cycling tests. These findings validate the effectiveness of the simplified DFT-based strategy for rapid DBM screening and support its potential in accelerating the development of high-performance thermoelectric devices.

4 Experimental

4.1 Materials synthesis

Polycrystalline n-type $Ag_2Se_{1.08}$ (hereafter referred to as Ag_2Se) was synthesized via a melting method. High-purity Ag powder (99.99%) and Se powder (99.99%) were weighed according to the stoichiometric ratio and sealed in evacuated quartz tubes. The sealed tubes were heated in a furnace to 1273 K over 6 h, held at this temperature for 12 h, then slowly cooled to 723 K and maintained at this temperature for 24 h, followed by furnace cooling to room temperature. The resulting ingots were subsequently ground via ball milling at 500 rpm for 3 h under an argon atmosphere. Dense Ag_2Se disks and DBM/Ag_2Se/DBM joints (Cu/Ag_2Se/Cu, Ni/Ag_2Se/Ni, and Ag/Ag_2Se/Ag) were fabricated by SPS under a uniaxial pressure of 50 MPa at 623 K for 5 min. Due to the higher melting point of Fe, Fe/Ag_2Se/Fe joints were sintered under the same pressure at 673 K for 10 min. For p-type MgAgSb synthesis, Mg powder (99.5%) and Ag powder (99.99%) were first weighed in a stoichiometric ratio of Mg:Ag = 1:1, loaded into a stainless steel jar inside an argon-filled glovebox, and ball-milled using a high-energy ball mill (SPEX-8000D) with two carbide balls (10.5 mm in diameter) for 10 h. Subsequently, Sb powder (99.5%) was added in the glovebox according to the final stoichiometric ratio of Mg:Ag:Sb = 1:1:1, followed by another 10 h of ball milling. Dense MgAgSb disks and Ag/MgAgSb/Ag joints were prepared by SPS under a uniaxial pressure of 80 MPa at 558 K for 5 min. The sintered samples were then annealed at 573 K for 30 min under a flowing gas mixture of 5% H_2 and 95% Ar to improve phase stability and homogeneity. NiSe and Ni_3Se_2 were synthesized via a melting process. Ni powder (99.9%) and Se powder (99.99%) were weighed according to the stoichiometric ratios, sealed in evacuated quartz tubes, and gradually heated to 1373 K. After holding at this temperature for 10 h, the tubes were furnace-cooled to room temperature. Cu_2Se was synthesized by high-energy ball milling stoichiometric amounts of Cu powder (99.9%) and Se powder (99.99%) in an argon-filled stainless steel jar using a SPEX-8000D mill for 6 h. Subsequently, DBM/Cu_2Se/DBM joints (DBM = Ag, Co, Ni, or Fe) were fabricated via SPS at 873 K for 5 min under 50 MPa uniaxial pressure. Electrically insulating mica paper was placed between the graphite mold and the powder during sintering.

4.2 Characterization and measurement

The phase composition and crystal structure of the sintered samples were characterized by XRD (Smart Lab 9 kW, Rigaku, Japan) using Cu Kα radiation. Microstructural analysis and elemental distribution were performed using SEM (ZEISS Sigma-500) equipped with EDS. The S and σ were simultaneously measured using a ZEM-3 system (Advance Riko). Thermal conductivity (κ) was calculated using the equation $\kappa = DdC_p$, where the thermal diffusivity (D) was measured with an LFA457 laser flash apparatus (Netzsch), the density (d) was determined by the Archimedes method, and the specific heat capacity (C_p) was estimated using the Dulong–Petit law. The ρ_c was tested using a custom-built four-probe measurement system, while the σ_s of the thermoelectric joints was evaluated using an electronic universal testing machine (Shenzhen SUNS Technology Stock Co., Ltd.). The CTE was measured using a Linseis DIL instrument (L75 HS160, Germany).

4.3 Device fabrication and measurement

The sintered Ni/Ag_2Se/Ni and Ag/MgAgSb/Ag joints were cut into leg segments with dimensions of 1.3 mm × 1.3 mm × 3.3 mm and 1.7 mm × 1.7 mm × 3.3 mm, respectively. Seven pairs of n-type and p-type thermoelectric legs were alternately arranged and assembled onto a copper-coated Al_3O_2 substrate (10 mm × 10 mm cross-

sectional area) using $Sn_{42}Bi_{58}$ solder (melting point: 411 K) at 448 K for 1 min. To ensure reliable electrical connections, copper wires were soldered to the hot-side Al_3O_2 substrate using $Sn_{63}Pb_{37}$ solder (melting point: 456 K), which prevented wire detachment during the thermoelectric leg assembly process. A detailed schematic of the Ag_2Se/MgAgSb thermoelectric cooler fabrication was provided in Fig. S27 in the ESM. The ΔT, Q_c, and COP of the cooler were measured using a commercial testing system (Shenzhen GST-TECH Intelligent Control Co., Ltd.).

4.4 Finite element simulation

The theoretical ΔT_{max} of the seven-pair Ag_2Se/MgAgSb thermoelectric cooler was obtained through three-dimensional finite element simulations using COMSOL Multiphysics. The simulations incorporated experimentally measured thermoelectric property data for both Ag_2Se and MgAgSb. The T_h of the device was fixed at 300 K, and the ρ_c for both n-type and p-type legs was set to 20 μΩ·cm^2. Based on the simulated ΔT_{max}, the optimal A_p/A_n and H were determined.

4.5 DFT calculations

In the framework of DFT calculations, the energy of 3 × 3 × 3 α-Ag_2Se supercell structure was calculated using the first-principles total energy projector-augmented wave method (Vienna *ab initio* simulation package, the VASP code) based on density functional theory [76]. The Perdew–Burke–Ernzerhof (PBE) [77] exchange-correlation function of the generalized gradient approximation (GGA) [78] and the projector-augmented-wave (PAW) were utilized for the calculations. The cutoff energy was 400 eV, the criterion for total energy was 10^{-6} eV, and all atomic positions were absolutely relaxed until the force was 0.01 eV·Å^{-1}. A 9 × 9 × 9 k-points mesh on the Brillouin zone (BZ) was employed for structure relaxation. The E_{Sub} of DBM atoms at the Ag site in Ag_2Se was calculated using the equation: $E_{Sub} = E(MAg_{15}Se_8) + E(Ag) - E(Ag_{16}Se_8) - E(M)$, where M = Cu/Ni/Fe; $E(MAg_{15}Se_8)$ and $E(Ag_{16}Se_8)$ are the total energies of subsitituted and pure supercell Ag_2Se, respectively; and $E(Ag)$ and $E(M)$ are the energies per atom for the elemental Ag and M, respectively. Similarly, the E_{Sub} of DBM atoms at the Cu site in Cu_2Se was calculated using the equation: $E_{Sub} = E(MCu_{15}Se_8) + E(Cu) - E(Cu_{16}Se_8) - E(M)$, where M = Ag/Co/Ni/Fe; $E(MCu_{15}Se_8)$ and $E(Cu_{16}Se_8)$ are the total energies of subsitituted and pure supercell Cu_2Se, respectively; and $E(Cu)$ and $E(M)$ are the energies per atom for the elemental Cu and M, respectively. The activation energy barriers for atom migration (E_{Mig}) to neighboring vacancies were determined using the climbing image nudged elastic band (CI-NEB) method with eight inserted images [79].

4.6 Phase diagram calculations

The thermodynamic modeling of the Ag–Ni–Se system was conducted using data from the Ag–Ni [73], Ag–Se [74], and Ni–Se [75] binary subsystems, with the corresponding binary phase diagrams provided in Fig. S17 in the ESM. The phases in the Ag–Ni–Se system were categorized into solution phases and intermetallic phases. The Gibbs energies of pure elements under the stable element reference were obtained from the Scientific Group Thermodata Europe (SGTE) by Dinsdale [80]. The solution phases based on the elements of Ag, Ni, Se, and liquid were described using substitutional solution model and associate solution model. The molar Gibbs energy of solution phase φ (G_m^{φ}) was given as follows

$$G_m^{\varphi} = \sum_i x_i^0 G_i^{\varphi} + RT\sum_i x_i \ln(x_i) + {}^{ex}G_m^{\varphi} \quad (1)$$

where x_i was the mole fraction of element i, ${}^0G_i^{\varphi}$ was the molar Gibbs energy of element i in state φ, R was the gas constant, T was the absolute temperature, and ${}^{ex}G_m^{\varphi}$ was the excess molar Gibbs energy that was given by the Redlich–Kister equation

$${}^{ex}G_m^{\varphi} = \sum_i \sum_{j>i} x_i x_j \sum_{v=0}^{n} (x_i - x_j)^v {}^vL_{i,j}^{\varphi} \quad (2)$$

where n and v were the highest degree and the degree of the polynomial, respectively. ${}^vL_{i,j}^{\varphi}$ was the temperature-dependent binary interaction parameter of the elements i and j, and expressed as

$${}^vL_{i,j}^{\varphi} = a + bT \quad (3)$$

All the intermetallic phases (β-Ag_2Se, α-Ag_2Se, Ni_3Se_2_LT, Ni_3Se_2_HT, Ni_6Se_5, NiSe, and $NiSe_2$, where LT and HT represented the low temperature and high temperature, respectively) were treated as a sublattice model, and the Gibbs energy was described based on the compound energy formalism (CEF) proposed by Mat Hillert [81]. The crystal structures of stable phases in the Ag–Ni–Se system were listed in Table S4 in the ESM and the thermodynamic parameters were listed in Table S5 in the ESM. The phase diagram presented in this work was calculated using Pandat software.

Electronic Supplementary Material: Supplementary material (DFT calculation results, SEM images, EDS results, XRD patterns, thermoelectric properties, and calculated phase diagrams) is available in the online version of this article at https://doi.org/10.26599/NR.2025.94907903.

Data availability

All data needed to support the conclusions in the paper are presented in the manuscript and the Electronic Supplementary Material. Additional data related to this paper may be requested from the corresponding author upon request.

Acknowledgements

This work was supported by the National Natural Science Foundation of China (Nos. U21A2054, 51961011, and 52273285). Z.-G. C. thanks the financial support from the Australian Research Council, HBIS Group-University of Queensland (HBIS-UQ) Innovation Centre for Sustainable Steel project, and the Queensland University of Technology (QUT) Capacity Building Professor Program. This work was enabled by using the Central Analytical Research Facility hosted by the Institute for Future Environments at QUT.

Declaration of competing interest

All the contributing authors report no conflict of interests in this work.

Author contribution statement

S. Y. Z. and X.-L. S.: Experimental design, data curation, project administration, validation, writing manuscript. Q. Z.: DFT calculations. J. S. L., Z. W. Z., Z. N. P., S. J. Z., J. G., and J.-L. C.: Data curation, project administration. M. L., W. Y. C., and T. S.:

Validation, resources. L. M. and Z.-G. C.: Project administration, writing – review & editing. All the authors have approved the final manuscript.

Use of AI statement

None.

References

[1] He, J.; Tritt, T. M. Advances in thermoelectric materials research: Looking back and moving forward. *Science* **2017**, *357*, eaak9997.

[2] Yang, Q. Y.; Yang, S. Q.; Qiu, P. F.; Peng, L. M.; Wei, T. R.; Zhang, Z.; Shi, X.; Chen, L. D. Flexible thermoelectrics based on ductile semiconductors. *Science* **2022**, *377*, 854–858.

[3] Jiang, B. B.; Yu, Y.; Cui, J.; Liu, X. X.; Xie, L.; Liao, J. C.; Zhang, Q. H.; Huang, Y.; Ning, S. C.; Jia, B. et al. High-entropy-stabilized chalcogenides with high thermoelectric performance. *Science* **2021**, *371*, 830–834.

[4] Chen, W. Y.; Shi, X. L.; Li, M.; Liu, T.; Mao, Y. Q.; Liu, Q. Y.; Dargusch, M.; Zou, J.; Lu, G. Q.; Chen, Z. G. Nanobinders advance screen-printed flexible thermoelectrics. *Science* **2024**, *386*, 1265–1271.

[5] Shi, X.; Zuo, Y.; Zhai, P.; Shen, J. H.; Yang, Y. Y. W.; Gao, Z.; Liao, M.; Wu, J. X.; Wang, J. W.; Xu, X. J. et al. Large-area display textiles integrated with functional systems. *Nature* **2021**, *591*, 240–245.

[6] Li, R. Y.; Ge, B. Z.; Zhou, C. J. Advanced porous thermoelectric materials: Design, construction, and application. *Nano Res.* **2025**, *18*, 94907308.

[7] Yan, Q. Y.; Kanatzidis, M. G. High-performance thermoelectrics and challenges for practical devices. *Nat. Mater.* **2022**, *21*, 503–513.

[8] Qin, Y. X.; Qin, B. C.; Wang, D. Y.; Chang, C.; Zhao, L. D. Solid-state cooling: Thermoelectrics. *Energy Environ. Sci.* **2022**, *15*, 4527–4541.

[9] Chen, W. Y.; Shi, X. L.; Zou, J.; Chen, Z. G. Thermoelectric coolers: Progress, challenges, and opportunities. *Small Methods* **2022**, *6*, 2101235.

[10] Liu, S. B.; Qin, B. C.; Zhao, L. D. PbSe thermoelectrics: Efficient candidates for power generation and cooling. *Adv. Energy Mater.* **2025**, *15*, 2404251.

[11] Chauhan, N. S.; Mori, T. Cooler, stronger, smaller: Improving thermoelectric cooling. *Natl. Sci. Rev.* **2025**, *12*, nwae445.

[12] Shi, X. L.; Wang, L. J.; Lyu, W. Y.; Cao, T. Y.; Chen, W. Y.; Hu, B. X.; Chen, Z. G. Advancing flexible thermoelectrics for integrated electronics. *Chem. Soc. Rev.* **2024**, *53*, 9254–9305.

[13] Wu, C. L.; Shi, X. L.; Wang, L. J.; Lyu, W.; Yuan, P.; Cheng, L. N.; Chen, Z. G.; Yao, X. D. Defect engineering advances thermoelectric materials. *ACS Nano* **2024**, *18*, 31660–31712.

[14] Wu, Z. H.; Zhang, S.; Liu, Z. K.; Mu, E. Z.; Hu, Z. Y. Thermoelectric converter: Strategies from materials to device application. *Nano Energy* **2022**, *91*, 106692.

[15] Han, H. W.; Zhao, L. J.; Wu, X. M.; Zuo, B.; Bian, S. N.; Li, T.; Liu, X. Y.; Jiang, Y. H.; Chen, C. Y.; Bi, J. L. et al. Advancements in thermoelectric materials: Optimization strategies for enhancing energy conversion. *J. Mater. Chem. A* **2024**, *12*, 24041–24083.

[16] Baskaran, P.; Rajasekar, M. Recent progress in thermoelectric devices and applications. *Chem. Eng. J.* **2025**, *506*, 159929.

[17] Wu, X. Z.; Lin, Y. J.; Han, Z. J.; Li, H.; Liu, C. Y.; Wang, Y. P.; Zhang, P. X.; Zhu, K.; Jiang, F.; Huang, J. et al. Interface and surface engineering realized high efficiency of 13% and improved thermal stability in $Mg_3Sb_{1.5}Bi_{0.5}$-based thermoelectric generation devices. *Adv. Energy Mater.* **2022**, *12*, 2203039.

[18] Cheng, J. X.; Yin, L.; Wang, X. Y.; Duan, S. C.; Zhao, P.; Ma, X. J.; Li, X. F.; Bao, X.; Zhi, S. Z.; Mao, J. et al. Realizing a superior conversion efficiency of ≈11.3% in the group IV–VI thermoelectric module. *Small* **2024**, *20*, 2312145.

[19] Miao, L. Y.; Zhang, Q.; Yuan, M. H.; Li, R. Y.; Wang, M.; Tan, X. J.; Wu, J. H.; Liu, G. Q.; Jiang, J. Thermo-electric-mechanical coupling selects barrier layer for advanced bismuth telluride thermoelectric generator. *Adv. Mater.* **2025**, *37*, 2503580.

[20] Qu, N.; Sun, Y. X.; Liu, Z. H.; Xie, L. J.; Zhu, Y. K.; Wu, H.; Chai, R. H.; Cheng, J. X.; Guo, F. K.; Zhang, Q. et al. Interfacial design contributing to high conversion efficiency in $Mg_3(Sb, Bi)_2/Bi_2Te_3$ thermoelectric module with superior stability. *Adv. Energy Mater.* **2024**, *14*, 2302818.

[21] Fu, Y. T.; Zhang, Q. H.; Hu, Z. L.; Jiang, M.; Huang, A. B.; Ai, X.; Wan, S.; Reith, H.; Wang, L. J.; Nielsch, K. et al. $Mg_3(Bi, Sb)_2$-based thermoelectric modules for efficient and reliable waste-heat utilization up to 750 K. *Energy Environ. Sci.* **2022**, *15*, 3265–3274.

[22] Liu, W. S.; Bai, S. Q. Thermoelectric interface materials: A perspective to the challenge of thermoelectric power generation module. *J. Materiomics* **2019**, *5*, 321–336.

[23] Yin, L.; Chen, C.; Zhang, F.; Li, X. F.; Bai, F. X.; Zhang, Z. W.; Wang, X. Y.; Mao, J.; Cao, F.; Chen, X. et al. Reliable n-type $Mg_{3.2}Sb_{1.5}Bi_{0.49}Te_{0.01}$/304 stainless steel junction for thermoelectric applications. *Acta Mater.* **2020**, *198*, 25–34.

[24] Liu, W. S.; Jie, Q.; Kim, H. S.; Ren, Z. F. Current progress and future challenges in thermoelectric power generation: From materials to devices. *Acta Mater.* **2015**, *87*, 357–376.

[25] Xing, T.; Song, Q. F.; Qiu, P. F.; Zhang, Q. H.; Gu, M.; Xia, X. G.; Liao, J. C.; Shi, X.; Chen, L. D. High efficiency GeTe-based materials and modules for thermoelectric power generation. *Energy Environ. Sci.* **2021**, *14*, 995–1003.

[26] Wu, X. Z.; Lin, Y. J.; Liu, C. Y.; Wang, Y. P.; Li, H.; Ge, B. H.; Liu, W. S. A high performance eco-friendly MgAgSb-based thermoelectric power generation device near phase transition temperatures. *Energy Environ. Sci.* **2024**, *17*, 2879–2887.

[27] Gu, M.; Bai, S. Q.; Wu, J. H.; Liao, J. C.; Xia, X. G.; Liu, R. H.; Chen, L. D. A high-throughput strategy to screen interfacial diffusion barrier materials for thermoelectric modules. *J. Mater. Res.* **2019**, *34*, 1179–1187.

[28] Yang, J. W.; Li, G. D.; Zhu, H. T.; Chen, N.; Lu, T. B.; Gao, J. L.; Guo, L. W.; Xiang, J. S.; Sun, P. J.; Yao, Y. et al. Next-generation thermoelectric cooling modules based on high-performance $Mg_3(Bi, Sb)_2$ material. *Joule* **2022**, *6*, 193–204.

[29] Xie, L. J.; Yin, L.; Yu, Y.; Peng, G. Y.; Song, S. W.; Ying, P. J.; Cai, S. T.; Sun, Y. X.; Shi, W. J.; Wu, H. et al. Screening strategy for developing thermoelectric interface materials. *Science* **2023**, *382*, 921–928.

[30] Yin, L.; Li, X. F.; Bao, X.; Cheng, J. X.; Chen, C.; Zhang, Z. W.; Liu, X. J.; Cao, F.; Mao, J.; Zhang, Q. CALPHAD accelerated design of advanced full-Zintl thermoelectric device. *Nat. Commun.* **2024**, *15*, 1468.

[31] Xie, L.; Ming, C.; Song, Q. F.; Wang, C.; Liao, J. C.; Wang, L.; Zhu, C. X.; Xu, F. F.; Sun, Y. Y.; Bai, S. Q. et al. Lead-free and scalable GeTe-based thermoelectric module with an efficiency of 12%. *Sci. Adv.* **2023**, *9*, eadg7919.

[32] Chu, J.; Huang, J.; Liu, R. H.; Liao, J. C.; Xia, X. G.; Zhang, Q. H.; Wang, C.; Gu, M.; Bai, S. Q.; Shi, X. et al. Electrode interface optimization advances conversion efficiency and stability of thermoelectric devices. *Nat. Commun.* **2020**, *11*, 2723.

[33] Liu, R. H.; Xing, Y. F.; Liao, J. C.; Xia, X. G.; Wang, C.; Zhu, C. X.; Xu, F. F.; Chen, Z. G.; Chen, L. D.; Huang, J. et al. Thermal-inert and Ohmic-contact interface for high performance half-Heusler based thermoelectric generator. *Nat. Commun.* **2022**, *13*, 7738.

[34] Fu, Y. T.; Ai, X.; Hu, Z. L.; Zhao, S. H.; Lu, X. F.; Huang, J.; Huang, A. B.; Wang, L. J.; Zhang, Q. H.; Jiang, W. Interface kinetic manipulation enabling efficient and reliable Mg_3Sb_2 thermoelectrics. *Nat. Commun.* **2024**, *15*, 9355.

[35] Wu, H.; Shi, X. L.; Duan, J. G.; Liu, Q. F.; Chen, Z. G. Advances in Ag_2Se-based thermoelectrics from materials to applications. *Energy Environ. Sci.* **2023**, *16*, 1870–1906.

[36] Liu, M.; Zhang, X. Y.; Zhang, S. X.; Pei, Y. Z. Ag_2Se as a tougher alternative to n-type Bi_2Te_3 thermoelectrics. *Nat. Commun.* **2024**, *15*, 6580.
[37] Mallick, M. M.; Franke, L.; Rösch, A. G.; Lemmer, U. Shape-Versatile 3D thermoelectric generators by additive manufacturing. *ACS Energy Lett.* **2021**, *6*, 85–91.
[38] Khan, J. A.; Moulik, R.; Bhattacharya, S.; Singh, J. P. Unraveling the synergistic role of kinks in zig-zag Ag_2Se nanorod arrays for high room-temperature zT and improved mechanical properties: Experimental and first-principles studies. *ACS Appl. Mater. Interfaces* **2024**, *16*, 64702–64713.
[39] Yang, D.; Shi, X. L.; Li, M.; Nisar, M.; Mansoor, A.; Chen, S.; Chen, Y. X.; Li, F.; Ma, H. L.; Liang, G. X. et al. Flexible power generators by Ag_2Se thin films with record-high thermoelectric performance. *Nat. Commun.* **2024**, *15*, 923.
[40] Lei, Y.; Qi, R. J.; Chen, M. Y.; Chen, H.; Xing, C. C.; Sui, F. R.; Gu, L. Y.; He, W. W.; Zhang, Y. G.; Baba, T. et al. Microstructurally tailored thin β-Ag_2Se films toward commercial flexible thermoelectrics. *Adv. Mater.* **2022**, *34*, 2104786.
[41] Kleinhanns, T.; Milillo, F.; Calcabrini, M.; Fiedler, C.; Horta, S.; Balazs, D.; Strumolo, M. J.; Hasler, R.; Llorca, J.; Tkadletz, M. et al. A route to high thermoelectric performance: Solution-based control of microstructure and composition in Ag_2Se. *Adv. Energy Mater.* **2024**, *14*, 2400408.
[42] Cao, T. Y.; Shi, X. L.; Hu, B. X.; Yang, Q. S.; Lyu, W. Y.; Sun, S.; Yin, L. C.; Liu, Q. Y.; Chen, W. Y.; Wang, X. D. et al. Advancing Ag_2Se thin-film thermoelectrics via selenization-driven anisotropy control. *Nat. Commun.* **2025**, *16*, 1555.
[43] Liang, Q.; Yang, D. W.; Xia, F. J.; Bai, H.; Peng, H. Y.; Yu, R. H.; Yan, Y. G.; He, D. Q.; Cao, S. W.; Van Tendeloo, G. et al. Phase-transformation-induced giant deformation in thermoelectric Ag_2Se semiconductor. *Adv. Funct. Mater.* **2021**, *31*, 2106938.
[44] Jiang, F.; Lin, C. H.; Cheng, J. X.; Yu, H. L.; Zhou, Y. F.; Ma, X. J.; Wu, L. Z.; Ye, S.; Chen, J.; Zhi, S. Z. et al. Prefer-oriented Ag_2Se crystal for high-performance thermoelectric cooling. *Adv. Funct. Mater.* **2025**, *35*, 2415000.
[45] Abusa, Y.; Yox, P.; Viswanathan, G.; Opare-Addo, J.; Sarkar, A.; Kyveryga, V.; Smith, E.; Lebedev, O. I.; Kovnir, K. A recipe for a great meal: A benchtop route from elemental se to superior thermoelectric β-Ag_2Se. *J. Am. Chem. Soc.* **2024**, *146*, 11382–11391.
[46] Cao, T. Y.; Shi, X. L.; Hu, B. X.; Liu, S. Q.; Lyu, W. Y.; Li, M.; Wang, S.; Chen, W. Y.; Liu, W. D.; Moshwan, R. et al. Indium-doping advances high-performance flexible Ag_2Se thin films. *Adv. Sci.* **2025**, *12*, 2500364.
[47] Zhang, Z. H.; Wang, F. C.; Lee, S. K.; Liu, Y.; Cheng, J. W.; Liang, Y. Microstructure characteristic, mechanical properties and sintering mechanism of nanocrystalline copper obtained by SPS process. *Mat. Sci. Eng. A* **2009**, *523*, 134–138.
[48] Wen, H. M.; Zhao, Y. H.; Zhang, Z. H.; Ertorer, O.; Dong, S. M.; Lavernia, E. J. The influence of oxygen and nitrogen contamination on the densification behavior of cryomilled copper powders during spark plasma sintering. *J. Mater. Sci.* **2011**, *46*, 3006–3012.
[49] Feng, B. Q.; Cheng, Y. R.; Liu, C. Y.; Gao, J.; Wu, G. J.; Bai, X. B.; Si, R. F.; Li, W. P.; Guo, Y.; Miao, L. Ag interstitial inhibition and phonon scattering at the ZnSe nano-precipitates to enhance the thermoelectric performance of Ag_2Se. *ACS Appl. Energy Mater.* **2023**, *6*, 2804–2811.
[50] Chen, J.; Sun, Q.; Bao, D. Y.; Liu, T. Y.; Liu, W. D.; Liu, C.; Tang, J.; Zhou, D. L.; Yang, L.; Chen, Z. G. Hierarchical structures advance thermoelectric properties of porous n-type β-Ag_2Se. *ACS Appl. Mater. Interfaces* **2020**, *12*, 51523–51529.
[51] Moser, Z.; Gąsior, W.; Pstruś, J.; Dębski, A. Wettability studies of Pb-free soldering materials. *Int. J. Thermophys.* **2008**, *29*, 1974–1986.
[52] Yin, L. M.; Xian, J. W.; Yao, Z. X.; Wang, G. Study of surface tension and wettability for three kinds of high Sn-containing lead-free solders. *Electron. Comp. Mater.* **2010**, *29*, 35–37,42.
[53] Arenas, M. F.; He, M.; Acoff, V. L. Effect of flux on the wetting characteristics of SnAg, SnCu, SnAgBi, and SnAgCu lead-free solders on copper substrates. *J. Electron. Mater.* **2006**, *35*, 1530–1536.
[54] Liashenko, O. Y.; Hodaj, F. Wetting and spreading kinetics of liquid Sn on Ag and Ag_3Sn substrates. *Scr. Mater.* **2017**, *127*, 24–28.
[55] Satyanarayan; Prabhu, K. N. Reactive wetting of Sn–2.5Ag–0.5Cu solder on copper and silver coated copper substrates. *J. Mater. Sci. Mater. Electron.* **2013**, *24*, 1714–1719.
[56] Rizvi, M. J.; Chan, Y. C.; Bailey, C.; Lu, H.; Islam, M. N.; Wu, B. Y. Wetting and reaction of Sn–2.8Ag–0.5Cu–1.0Bi solder with Cu and Ni substrates. *J. Electron. Mater.* **2005**, *34*, 1115–1122.
[57] Protsenko, P.; Terlain, A.; Traskine, V.; Eustathopoulos, N. The role of intermetallics in wetting in metallic systems. *Scr. Mater.* **2001**, *45*, 1439–1445.
[58] Lin, Q. L.; Ye, C. S.; Sui, R.; Ci, W. J. Wetting of amorphous and partial crystalline $Co_{73}Si_{10}B_{17}$ by Sn and Sn-based lead-free solders. *Microelectron. Reliab* **2019**, *98*, 112–118.
[59] Kyaw, T. T.; Tunthawiroon, P.; Kanlayasiri, K.; Yamanaka, K.; Chiba, A. A study on wettability and formation of intermetallic phase between Co–Cr–Mo alloy and Sn-solder used as a potential under bump metallization for flip-chip packages. *Intermetallics* **2020**, *125*, 106875.
[60] Liu, Y.; Yu, W. Y.; Wang, C. S.; Zhang, J. The wetting behavior of Al/Sn under ultrasonic action. *Mater. Today Commun.* **2023**, *36*, 106499.
[61] Huan, P. C.; Tang, X. X.; Sun, Q.; Akira, K.; Wang, X. N.; Wang, J.; Wang, J. L.; Wei, X.; Di, H. S. Comparative study of solder wettability on aluminum substrate and microstructure-properties of Cu-based component/aluminum laser soldering joint. *Mater. Des.* **2022**, *215*, 110485.
[62] Zhan, S. P.; Bai, S. L.; Qin, B. C.; Zhu, Y. C.; Wang, S. Q.; Liu, D. R.; Hong, T.; Gao, X.; Zheng, L.; Wen, Y. et al. High carrier mobility promotes in-plane thermoelectric performance of n-type $PbSnS_2$ crystals. *Adv. Funct. Mater.* **2024**, *34*, 2406428.
[63] Liu, S. B.; Qin, Y. X.; Wen, Y.; Shi, H. N.; Qin, B. C.; Hong, T.; Gao, X.; Cao, Q.; Chang, C.; Zhao, L. D. Efforts toward the fabrication of thermoelectric cooling module based on n-type and p-type PbTe ingots. *Adv. Funct. Mater.* **2024**, *34*, 2315707.
[64] Wang, S. Q.; Bai, S. L.; Chen, P. P.; Zhan, S. P.; Tian, Y.; Wang, L.; Liu, D. R.; Peng, J. Y.; Li, Y. C.; Gao, D. Z. et al. Off-center distortions and resonant levels: A pathway to enhance power generation and thermoelectric cooling in PbSe crystals. *J. Am. Chem. Soc.* **2025**, *147*, 15827–15837.
[65] Xu, W. L.; Al-Maythalony, B. A.; Li, J.; Li, X.; Fu, L. W.; Xu, B. Amorphous carbon-modulated $Mg_3(Bi, Sb)_2$ and electron-poor CdSb for ultralow-cost te-free refrigeration modules. *Adv. Funct. Mater.* **2025**, *35*, 2414194.
[66] Liu, S.; Bai, S. L.; Wen, Y.; Lou, J.; Jiang, Y. Z.; Zhu, Y. C.; Liu, D. R.; Li, Y. C.; Shi, H. N.; Liu, S. B. et al. Quadruple-band synglisis enables high thermoelectric efficiency in earth-abundant tin sulfide crystals. *Science* **2025**, *387*, 202–208.
[67] Chen, J.; Sun, Q.; Bao, D. Y.; Tian, B. Z.; Wang, Z. G.; Tang, J.; Zhou, D. L.; Yang, L.; Chen, Z. G. Simultaneously enhanced strength and plasticity of Ag_2Se-based thermoelectric materials endowed by nano-twinned CuAgSe secondary phase. *Acta Mater.* **2021**, *220*, 117335.
[68] Tee, S. Y.; Tan, X. Y.; Wang, X. Z.; Lee, C. J. J.; Win, K. Y.; Ni, X. P.; Teo, S. L.; Seng, D. H. L.; Tanaka, Y.; Han, M. Y. Aqueous synthesis, doping, and processing of n-type Ag_2Se for high thermoelectric performance at near-room-temperature. *Inorg. Chem.* **2022**, *61*, 6451–6458.
[69] Huang, S. J.; Wei, T. R.; Chen, H. Y.; Xiao, J.; Zhu, M.; Zhao, K. P.; Shi, X. Thermoelectric Ag_2Se: Imperfection, homogeneity, and reproducibility. *ACS Appl. Mater. Interfaces* **2021**, *13*, 60192–60199.
[70] Mi, W. L.; Qiu, P. F.; Zhang, T. S.; Lv, Y. H.; Shi, X.; Chen, L. D. Thermoelectric transport of Se-rich Ag_2Se in normal phases and phase transitions. *Appl. Phys. Lett.* **2014**, *104*, 133903.

[71] Gu, M.; Bai, S. Q.; Xia, X. G.; Huang, X. Y.; Li, X. Y.; Shi, X.; Chen, L. D. Study on the high temperature interfacial stability of Ti/Mo/$Yb_{0.3}Co_4Sb_{12}$ thermoelectric joints. *Appl. Sci.* **2017**, *7*, 952.
[72] Zhang, Q. H.; Liao, J. C.; Tang, Y. S.; Gu, M.; Liu, R. H.; Bai, S. Q.; Chen, L. D. Interface stability of skutterudite thermoelectric materials/$Ti_{88}Al_{12}$. *J. Inorg. Mater.* **2018**, *33*, 889–894.
[73] Shi, Y. C.; Hu, B.; Jin, C. G.; Luo, M.; Liu, S. H.; Du, Y.; Hu, J. Q. Experimental investigation and thermodynamic modeling of phase equilibria in the Ag–Ni–Zr ternary system. *Phys. Chem. Chem. Phys.* **2022**, *24*, 22263–22277.
[74] Hutabalian, Y.; Chen, S. W.; Gierlotka, W. Phase equilibria of binary Ag–Se and ternary Ag–Pb–Se systems. *Calphad* **2024**, *86*, 102709.
[75] Zobač, O.; Buchlovská, K.; Pavlů, J.; Kroupa, A. Thermodynamic description of binary system nickel–selenium. *J. Phase. Equilib. Diff.* **2021**, *42*, 468–478.
[76] Kresse, G.; Furthmüller, J. Efficient iterative schemes for *ab initio* total-energy calculations using a plane-wave basis set. *Phys. Rev. B* **1996**, *54*, 11169–11186.
[77] Constantin, L. A.; Pitarke, J. M.; Dobson, J. F.; Garcia-Lekue, A.; Perdew, J. P. High-level correlated approach to the jellium surface energy, without uniform-gas input. *Phys. Rev. Lett.* **2008**, *100*, 036401.
[78] Perdew, J. P.; Burke, K.; Ernzerhof, M. Generalized gradient approximation made simple. *Phys. Rev. Lett.* **1996**, *77*, 3865–3868.
[79] Henkelman, G.; Uberuaga, B. P.; Jónsson, H. A climbing image nudged elastic band method for finding saddle points and minimum energy paths. *J. Chem. Phys.* **2000**, *113*, 9901–9904.
[80] Dinsdale, A. T. SGTE data for pure elements. *Calphad* **1991**, *15*, 317–425.
[81] Hillert, M. The compound energy formalism. *J. Alloy. Compd.* **2001**, *320*, 161–176.